Investigation of gas/shear-thinning liquids flow at high throughput in microchannels with the aim of producing biosourced foam

M. Laporte, Agnès Montillet, A. Belkadi, D. Della Valle, C. Loisel, A. Riaublanc, J.L. Hauser

Investigation of gas/shear-thinning liquids flow at high throughput in microchannels with the aim of producing biosourced foam.

M. Laporte[1,2], A. Montillet[1,*], A. Belkadi[1,4], D. Della Valle[2,4], C. Loisel[1,2], A.Riaublanc[3], J. L. Hauser[1]

[1]*LUNAM Université, Université de Nantes, CNRS, GEPEA, UMR6144, BP 406, 44602 Saint-Nazaire (France),*

[2]*ONIRIS, BP 82225, 44322 Nantes (France),*

[3]*UR1268 Biopolymères, Interactions, Assemblages, INRA, 44316 Nantes (France),*

[4]*LUNAM Université, Université de Nantes, CNRS, LTN, UMR6607, BP 50609, 44306 Nantes (France)*

[*]*Corresponding author : agnes.montillet@univ-nantes.fr,*

Abstract

The context of this work is to explore the possibility of making bio-sourced foams at high throughput in microsystems. A fundamental element for the development of new technologies based on biphasic flows in microchannels is a good characterization and knowledge of hydrodynamics. In this contribution, cross slot microsystems are tested as a promoter for the formation of train of bubbles in aqueous solutions of xanthan gum. A flow chart is proposed to present the conditions allowing a dispersed flow regime; i.e. the conditions guaranteeing the complete incorporation of the gas into the liquid phase (no gas pocket) and then the control of the void fraction. The foaming is studied under potential industrial conditions, i.e. operating with liquid flow rates up to 24 L/h. High speed imaging within the channels reveals that the mechanism of formation of bubbles is related to flow focusing. Bubbles are generated alternatively from each of the two opposite gas inlets. Using whey protein isolate to enhance foaming points out that the bubble size may be reduced along a long channel by

tip streaming. The effect of the modulation of the viscosity of the liquid base (xanthan gum content) is also discussed.

Keywords: Microchannels, biphasic flow, high throughput, high speed visualization, bubble train, non-Newtonian liquids.

Highlights

Design of a foaming process by using microchannels for food or cosmetic applications

Test of two cross slot microsystems at high biphasic throughput (Q_L= 4.2-24 L/h)

Presentation of flowcharts for nitrogen dispersed in aqueous xanthan gum solutions

Characterization of genesis of bubble and bubble distribution along the channel

Tip streaming phenomenon is observed in the microchannel

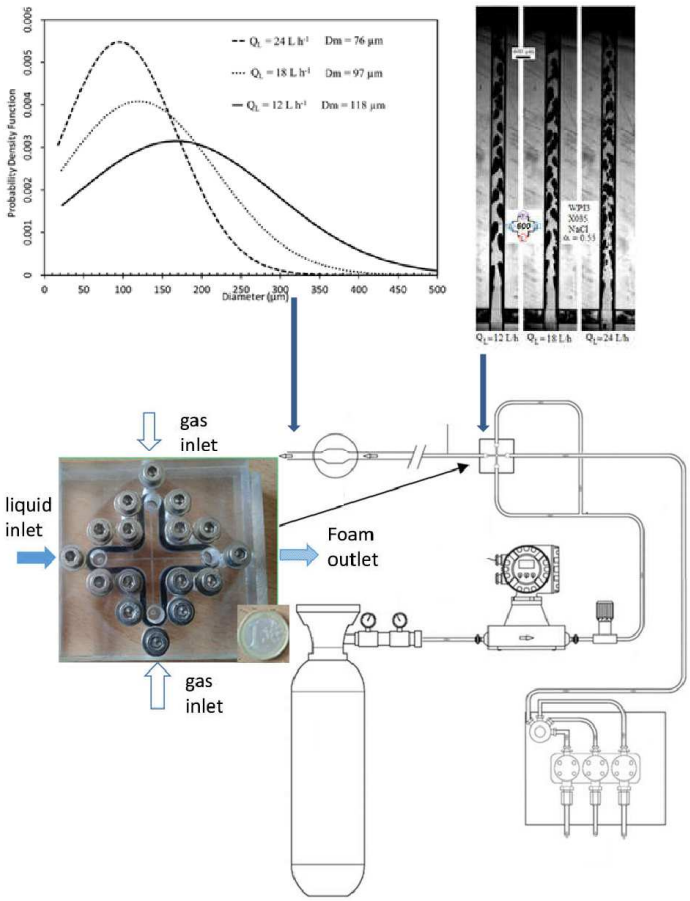

Graphical Abstract

1. Introduction

In the last twenty years, miniaturized systems have attracted growing interest in chemical engineering processes, but also in other fields, and considerable progresses have been made in their knowledge and industrial development. The use of microchannels is generally part of an intensification purpose aiming to improve the efficiency, thanks to the easy control of transfer settings, as well as the safety of the process, for the sake of industrial transition to “green processes” (Poux et al. 2015). The microchannels proved themselves in areas as diverse as chemical, cosmetic and pharmaceutical industries, especially in improving the quality of the mixture (Nguyen 2011). The size reduction also coincides with the compacity concept, in the good trend for industrial plants optimization. In addition, less cumbersome processes allow the establishment of parallel production methods improving the delays. Another advantage offered by microsystems is a quasi-immediate steady state

and a perfect reproducibility of the characteristics of the products. A large range of geometries and principles of operation of micromixers is available in the literature, each kind of apparatus presenting its own interest.

Micrometer-sized channels provide a high specific area, facilitating heat and mass transfers. Indeed, for a micro reactor it may vary between 10 000 - 50 000 m^2 per m^3, whereas in the case of conventional reactors, it remains around 100 $m^2.m^{-3}$ (Kockmann 2008). On the other hand, traditionally neglected phenomena in conventional processes may have a significant effect in microchannels, as surface micro-roughness, surface tension phenomena and clogging risk; replacement cycle or regular cleaning are usually needed. A strong limitation in open loop processes is to ensure acceptable pressure drops, both by the design and the operating conditions.

All these aspects must be taken into account in the development of micromixers. Optimal designs heavily rely on the flow regimes (laminar, turbulent and transient) and pressure drop correlations. Understanding of the parameters governing the flow is thus the subject of recent research in microfluidics (Kumar et al. 2011; Galletti et al. 2012). The micro-mixers are able to mix efficiently over a quite large range of experimental conditions. However, they are generally associated with several constraints and limitations that make it difficult to adapt to the industrial level. Therefore, there is no universal micro-mixer which can satisfy all the requirements of microsystems technology and that would suit for all kinds of applications.

The mixing efficiency is directly linked to the flow regime and the geometry. T and cross geometries are the most studied, as they are most appropriate for the transfer intensification. In these geometries, the mixing quality improves with the increase of Reynolds numbers and the occurrence of recirculation zones after the impact of fluids (Srisamran and Devahastin 2006). The magnitude of these vortices increases with the Reynolds number. These preferential recirculation zones have been observed in microchannels with cross geometry (Huchet et al. 2008). These cross shaped micromixers are also designated in the literature as cross slot. Although little studied from the point of view of design, they exhibit excellent transfer performance due to the contacting of the fluids in an impact zone causing significant shear (Srisamran and Devahastin 2006). It might be added that more intense turbulent zones are observed in a cross micromixer than in a T, as shown in the experiments from Huchet et al. (2008) and Ait Mouheb et al. (2010), by using particle imaging velocimetry (PIV) and electrochemical method. For this, the cross geometry was retained in the present work.

For biphasic applications, the flow pattern is the major feature for the foaming performances. In order to control the flow, the knowledge of the influence of the geometry and size of the micro-mixers, as well as that of the flow rates, and gas and liquid properties is then essential. Generally, the flow pattern is determined by the ratio of gas and liquid flow rates (Garstecki et al. 2006), but till now, this knowledge is far to be unified, and only specific features can be found in the literature. For instance, it is noteworthy that the majority of the tests presented in the literature were performed with low air and water flowrates (~µL to mL per hour). Finally, it is clear that further experiments are needed to clarify flow pattern for higher throughputs, to fully exploit the potential of this technology for gas/liquid mixing.

The present study is performed with cross slot geometries, under conditions that match industrial requirements, *i.e*. fluid flow rates of several liters per hour. For the sake of food or cosmetic applications, the liquid is formulated with bio-sourced compounds: whey protein isolate (WPI) is used as foaming agent and xanthan (XG) as a thickening agent. The liquid base is non-Newtonian with a viscous shear-thinning behavior, and the gas phase is nitrogen (N_2). Biphasic flow charts are established, so as to characterize the proper working domain, meaning flow conditions that guarantee a dispersed flow pattern, in which it is possible to control the void fraction in the foam by the flowrates. The originality of this work is to observe and analyze the formation of bubble train in the impact zone of these two fluids, thanks to high speed visualization. The structure of the gas/liquid flow is described at different fluids flow rates. The influence of the fluid viscosity on the bubble formation is qualitatively discussed.

2. Materials and methods

2.1. WPI-XG solutions

As the general context of this work is to explore the possibility of making bio-sourced foams, the foams are prepared from aqueous solutions of whey protein isolates, at different concentrations of xanthan gum in order to modulate the viscosity. The WPI are used for their surfactant properties while XG acts as thickener. Xanthan gum (Cargill, Baupte, France) provides high viscosities to aqueous solutions at low concentrations, with a strong shear thinning behavior (Sworn, 2011). In food applications, xanthan gum can be used up to a concentration 0.5% (weight per total weight). The particular rheology of aqueous solutions of xanthan gum (see 2.1.1) makes

this thickener interesting for the presently investigated foaming process: their highly shear thinning behavior allows to implement high velocity in the small sections of the microchannels without inducing prohibitive pressure losses. WPI powder, Prolacta95, is purchased from Lactalis Ingredients (Bourgbarré, France). Whey protein isolates have a molecular weight of about molecular weight about 14-18 kDa. They are known to have foaming abilities that are even better than those of aggregated WPI (Famelard et al. 2011).

Three WPI-XG solutions are tested in this work. Their formulation includes 3 wt% of WPI as well as mass contents of respectively 0.2, 0.35 and 0.5 wt% of xanthan gum. The tested range of xanthan content is thus coherent with usual industrial practices. These solutions are designated as WPI3X02, WPI3X035 and WPI3X05 respectively. A fourth solution is obtained by adding NaCl (0.2 M) to WPI3X035 to test the eventual effect of the ionic strength on the conformation of the protein and/or xanthan gum. Compositions of these solutions are recapped in Table 1. At these concentrations, both biopolymers do not interact and are soluble in water (Benichou et al. 2007). The solutions are prepared by dispersing the powders in batches of about 20 L in a cylindrical mixing vessel (Guedu, Lavergne, France) at a controlled temperature (40°C) under low speed stirring (50 rpm) during 5 hours. The pH is adjusted to 7, by addition of 0.1M NaOH solution, for better protein solubilization (Guimarães Pelegrine and de Moraes Santos Gomes 2008). The batches are then kept at 4°C for 24h to ensure complete hydration of the polymers.

2.1.1. *Viscosity*

The viscosity of the WPI-XG mixtures is characterized for each batch using the AR-1000N rheometer (TA Instruments, USA) with cone-plate geometry (60 mm diameter, 4° cone angle), sweeping the shear rate $\dot{\gamma}$ in the range [0.3 s^{-1}- 700 s^{-1}]. As all the tests are performed at room temperature, measurements are made at 20°C.

The viscosity of the solutions is affected by the XG concentration, while the addition of sodium chloride at a given XG concentration slightly decreases the viscosity. As formerly pointed out by Sworn (Sworn, 2000), flow curves of xanthan gum solution exhibit a shear thinning behavior that can be fitted with a power law for shear rates between 0.3 and 700 s^{-1}, as seen in Fig. 1:

$$\tau = K\,\dot{\gamma}^{n} \qquad (1)$$

Where τ is the shear stress, K, the flow consistency and n, the flow index.

According to Sworn (Sworn, 2000), aqueous solutions of xanthan are also characterized by two levelling off of the viscosity that are designated as the upper and lower Newtonian regions. As an example, the lower Newtonian

region of 0.5% xanthan gum solution is observed by Sworn (Sworn, 2000) for shear rates higher than 10^5 s^{-1}, where the viscosity is about 1.7 mPa s. In the present experimental work, the range of shear rate encountered in the outlet channels is [0.62-4.3] 10^5 s^{-1} (Table 2) which indicates that the aqueous solution of xanthan may exhibit a Newtonian behavior and a small apparent viscosity in the microchannels**.** In the range of shear rates investigated in the microchannels, the apparent viscosity is then estimated using Equation 2, where μ_0 is the viscosity of the solvent (water) :

$$\mu_L = K\,\dot{\gamma}^{n-1} + \mu_0 \qquad (2)$$

The constant μ_0 accounts for the second Newtonian plateau trend. Although it is not accurately determined yet, this term avoids unrealistic viscosity values given by the Oswald-deWaele model at very high shear rates.

2.1.2. Surface tension

The surface tension σ of the solutions is measured with a tensiometer (K12, Krüss GmbH, Germany) using the Wilhelmy's plate method at 20°C during 3h. At a constant WPI concentration, the surface tension is 44 ± 1 $mN.m^{-1}$ at long time (equilibrium value) for all the solutions. It was verified that neither xanthan gum (Dickinson and Walstra 2011) nor sodium chloride changes the interfacial tension. As mentioned in the literature (Lee et al. 2012) the interfacial tension of aqueous solution of xanthan at low content (0.1 -0.5 wt%) is about 70 $N\ m^{-1}$, provided that no impurity is introduced with the xanthan gum. The composition and properties of the solutions are gathered in **Table 1**.

177

178

179

180 **Table 1.**Composition and properties of the aqueous solutions, 20°C

Content and properties of aqueous solutions → Designation of aqueous solution ↓	WPI (wt%)	XG (wt%)	NaCl 0.2M (wt%)	ρ_L (kg.m^{-3}) ± 3%	K (Pa.s^n) ± 6%	n (-) ± 5%	σ (N.m^{-1}) ± 3%
WPI3X02	3	0.2	0	1032	0.89	0.29	0.044
WPI3X035NaCl	3	0.35	1.2	1046	2.2	0.24	0.044
WPI3X035	3	0.35	0	1034	3.1	0.20	0.044
WPI3X05	3	0.5	0	1035	5.2	0.14	0.044

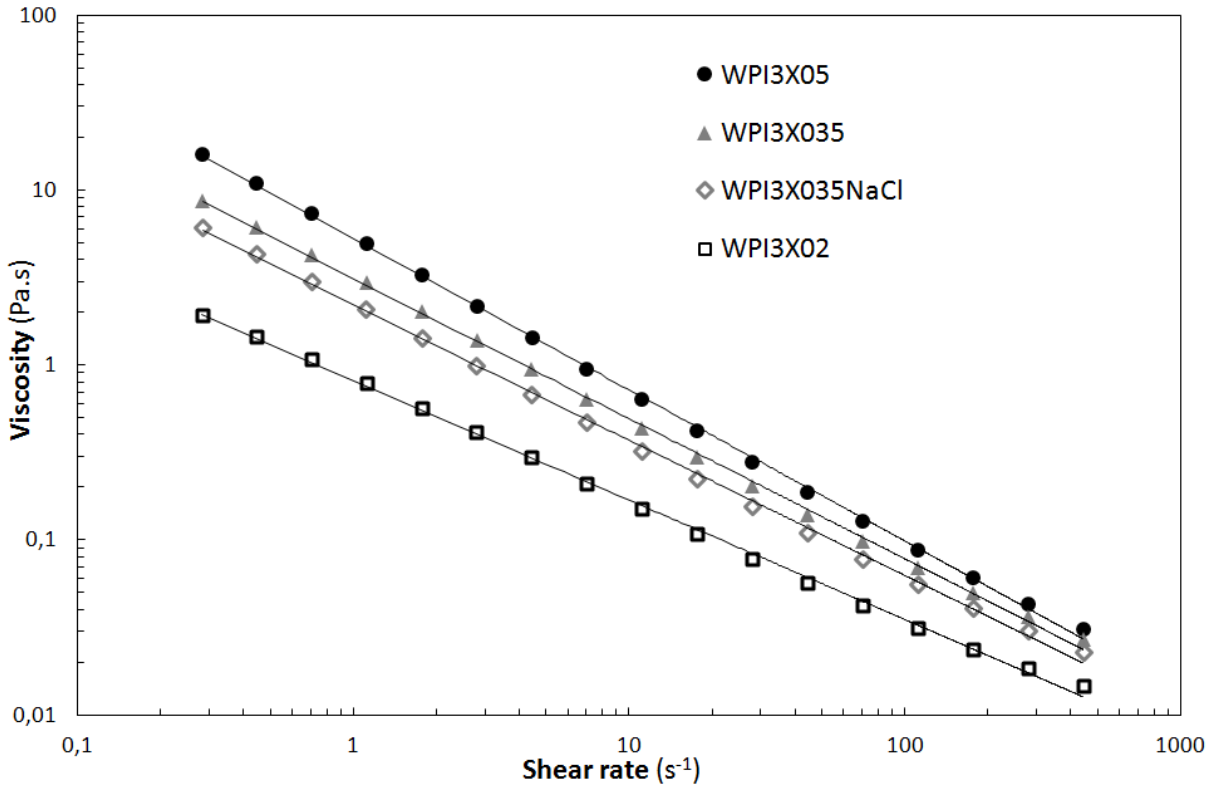

Fig.1 : Flow curves at 20°C with the four WPI-XG liquid solutions tested in this work.

2.2. *Microchannels*

2.2.1. *Hydraulic loop*

The experiments were carried out in two micro devices with similar geometry. Both are cross-shaped (so called cross slot geometry), composed of four branches with a square section and the same length (20 mm). As explained in fig.2, two opposite branches are used for the gas inlet, one for the liquid inlet and the last one for the foam outlet. The fluids are injected perpendicularly to the plane of the channels, thus in the plane of the microsystem (**Fig.3**). The two systems differ in the channel section side: 500 µm for the first one, and 600µm for the second one. Both devices were fabricated in our lab from a polymethylmethacrylate (PMMA) plate (60×60×15mm), by precision milling, and threaded into another PMMA plate (90×60×15mm). According to the literature, the value of surface energy of PMMA is about 40 $mJ.m^{-2}$ at 20°C. The two plates are easily removable, ensuring an easy cleaning if necessary. They are transparent and resist to pressures up to 20 bars at least. Sealing is ensured by a gasket and systems of screws, bolts and lock nuts.

Fig.2. displays the whole experimental loop. A piston pump (AP Trix™, Armen, France) is used to feed the microchannels with the liquid and to control its flow rate. Gas is N_2 (provided by Air liquid, France). The gas flow rate is measured using a Coriolis mass flow-meter (Promass 80, Endress+Hausser™, Switzerland); according to the manufacturer, the maximal uncertainty is ± 0.75%. An analog pressure sensor (Gems sensors, USA), with adjusted measuring range up to 25 bars, is located before the gas injection. According the manufacturer, the uncertainty of the measured pressure is 0.25% of the full scale. Teflon tubes (FEP, Inlet Diameter ID = 0.156 cm) were employed to connect the microchannel device with gas and liquid supplies. The same kind of tube (FEP, ID = 0.156 cm), of 3.70 m long, is used at the outlet of the microsystem in order to avoid a too large variation of the hydraulic diameter and to ensure a progressive decrease of the pressure. A thermocouple (Type K, Omega®, France) is used to record the temperature of the foam in this tube; it is set after the outlet of the microsystem. Another tube (PVC, ID = 1 cm) of 4.30 m long is added to ensure a back pressure with a smooth pressure decrease, and to connect the visualization cell.

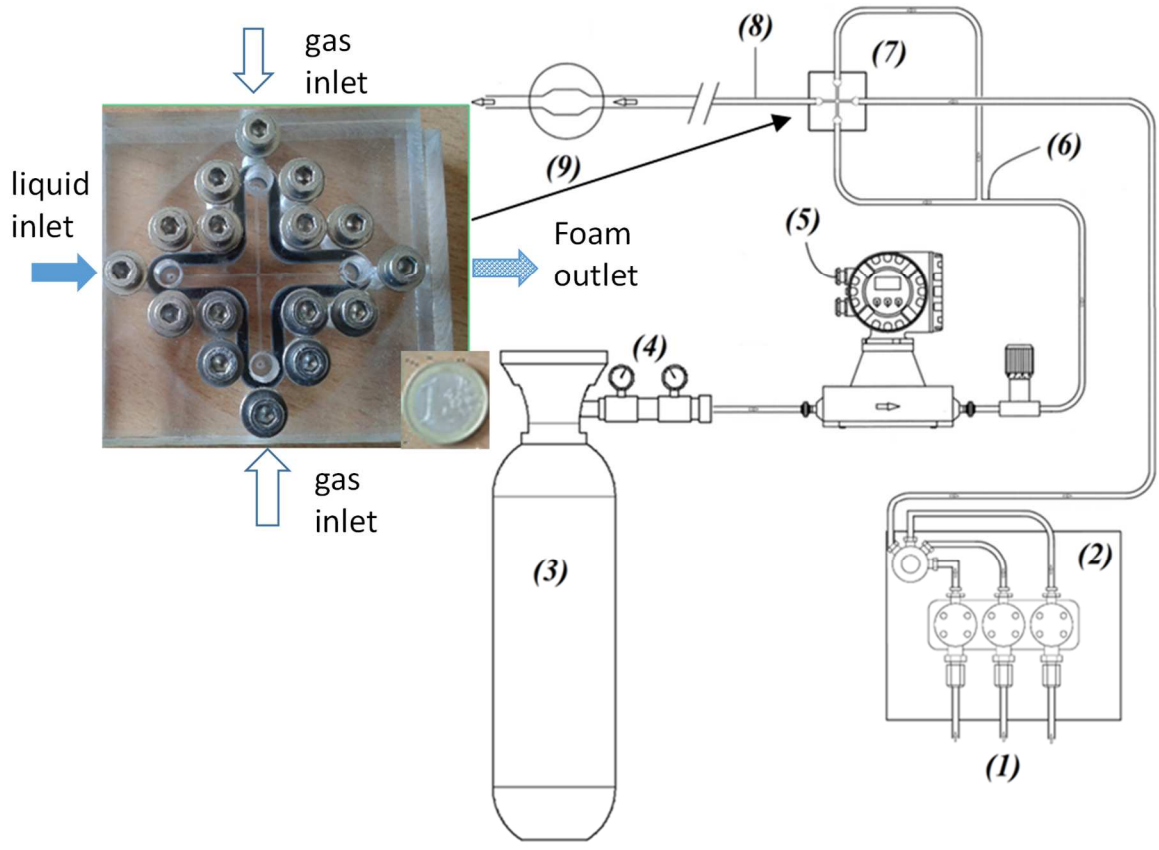

Fig.2. Experimental rig : (1) Liquid feed; (2) Pump; (3) Gas supply; (4) Gas expander; (5) Mass gas flow meter; (6) Absolute gas pressure sensor; (7) Microchannels; (8) Temperature sensors; (9) Visualization cell for foam at the outlet of the process.

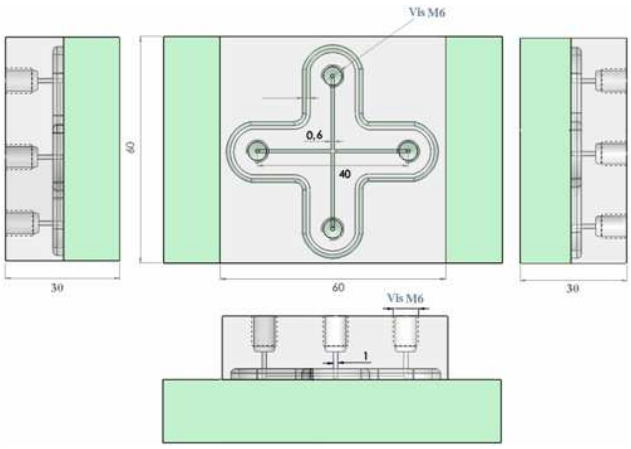

Fig.3: plan of the microsystem cross 600 (dimensions are given in mm).

2.2.2. Image capture with a high speed camera

Image sequences are taken from a speed camera HighSpeedStar 6 (LaVision, Göttingen, Germany) provided with lenses, that can reach a maximum frequency of 675 000 frames per second (fps). In our tests, the flow is observed in the outlet channel, in which the two fluids flow. The refractive index of the PMMA is 1.48 and that of water is 1.33. The difference of refractive index is negligible, as previously demonstrated by several authors (Besagni et al., 2016). A rate of 5000 frames per second is captured with an acquisition time of 1µs. Thus, the time span between two images is 0.2ms. At the chosen frequency, the image definition is 1024x320 pixels^2 and the resolution is 16.4 µm per pixel. With the obtained magnification, about 15 mm of channel length can be observed in a single field of view. As formerly mentioned, the total length of the outlet channels is 20 mm but it is not possible to observe its entirety due to the pipe at the outlet that clutters the visualization. The images are recorded from the camera using a computer equipped with image acquisition software DaVis (LaVision, Germany).

2.3. Bubble size distribution at the outlet of the process

The foam can be observed at the output of the whole process at atmospheric pressure through a PMMA transparent visualization cell placed under a camera which allows image acquisition of 4 x 5 mm field of view with 5 M pixels definition. The resulting images are analyzed with the software Visilog™7.0 (Noesis, France) to provide the experimental values of bubbles size distribution. At least 300 bubbles per sample were needed to converge to the true probability density function (pdf) (Vigneau et al. 2000). The log-normal law fairly fits the experimental distribution. The mean square deviation (MSD) remains similar for each trial, i.e. around 70%.

Therefore, the log-modal diameter D_m is computed from the experimental diameter series to represent the typical size of the bubbles.

2.4. Gas fraction

The volume fraction is one of the most important control parameters used to characterize the mixing in biphasic flows. The gas incorporation and breakup depends, among other dynamic parameters, on the ability of the protein to lower the surface tension between liquid and gas during foaming. In the perfectly dispersed regime, assuming a zero slip velocity between the two phases, the outlet gas volume fraction α of the foam is determined from the liquid and gas volumetric flow rates at ambient, respectively Q_L and Q_G and reads:

$$\alpha_{theoretical} = \frac{Q_G}{Q_G + Q_L} \quad (3)$$

The experimental void fraction is deduced from the amount of gas incorporated in the foam. It is given from the experimental overrun OV which represents the foaming expansion rate and which is expressed in percentage. It is calculated from the weight, W_L, of the liquid solution filling a given receptacle and that, W_F, of the foam filling the same receptacle, with 0.5% deviation.

$$OV\ (\%) = 100\frac{W_L - W_F}{W_F} \quad (4)$$

$$\alpha_{experimental} = \frac{OV\%}{100 + OV\%} \quad (5)$$

3. Results and discussion

The purpose of this work is to characterize the structure and typology of the gas/liquid flow in the cross 600 and in the cross 500. Flow rates of fluids are varied, with the volume liquid flow rate Q_L ranging between 4.2 and 24 $L.h^{-1}$. As formerly mentioned, the composition of the liquid base is varied by modulating the amount of xanthan and using or not sodium chloride. In the absence of or at low shear rate, the apparent viscosities of the different solutions are significantly different (Figure 1). At the flow conditions tested in the microchannels (Table 2), for which the lower Newtonian region is approached or reached, this difference is probably very tiny or negligible. This is a crucial point: the particular shear thinning character of aqueous solutions of xanthan gum explains that such fluids can be easily handled in microsystems at high throughput.

The operating conditions for both fluids are collected in Table 2; they are calculated considering the conditions at the outlet channel of the microsystem (up flow the back pressure tube).

At the micrometric scale, the flow behavior can be described by several dimensionless numbers. They account for six variables, density ρ, viscosity μ, surface tension σ, hydraulic diameter D_H, superficial velocity U_s and acceleration of gravity g, that are based on the fundamental units of mass, length and time. The Reynolds number is defined as the ratio of inertial forces to viscous ones:

$$Re = \frac{\rho D_h U_s}{\mu} \tag{6}$$

The capillary number is the ratio of the viscous forces and the surface tension:

$$Ca = \frac{\mu U_s}{\sigma} \tag{7}$$

The Weber number represents the ratio of inertial forces and surface tension:

$$We = \frac{\rho U_s^2 D_h}{\sigma} \tag{8}$$

And Bond number takes into account the ratio of gravitational forces and surface tension:

$$Bo = \frac{\rho g D_h^2}{\sigma} \tag{9}$$

From these definitions, it appears that the effect of surface tension forces become dominant over the gravitational forces as the size of the channel decreases.

The wall shear rate, $\dot{\gamma}$, is estimated in the outlet microchannel, making the assumption that the flow is laminar and established, using the following equation for ducts of square section:

$$\dot{\gamma} = \frac{7.115\,(U_{s,L}+U_{s,G})}{D_h} \tag{10}$$

Where $U_{s,L}$ and $U_{s,G}$ are respectively the liquid and gas superficial velocities.

Values of Re, Ca, We and Bo are that are reported in Table 2 for the liquid phase, are calculated considering WPI3X035 only (ρ_l= 1035 kg m^{-3}, μ_l is calculated from Eq. 2). Concerning the gas phase, which is nitrogen, μ_g = 1.75×10^{-5} Pa.s at 20°C and at atmospheric pressure (P_{atm}). For pressures below 35 bars, the pressure effect on the viscosity of the gas is negligible (Crane 1988).

Given the dimensionless numbers, it appears that the flow regime is laminar and that the inertial forces outweigh the viscous forces in the flow (Re >> 1), while Bo << 1 and Ca <1. According to the literature (Engler et al. 2004; Soleymani et al. 2008; Srisamran and Devahastin 2006; Ait Mouheb 2010), the Reynolds number range explored here corresponds to a favorable range regarding increased transfer in microchannels. Indeed, if one refers to the liquid-liquid mixing in these systems, beyond Re = 100 to 150, the quality of the mixture is greatly

increased. It may be added that the trials with the two-phase system used in this study correspond to an unexplored situation in the literature.

The residence time in the microchannel output ranges between 0.1 and 1.5 ms with liquid flow rates between 2 and 24 $L.h^{-1}$ and gas flow rates between 2 and 50 $L.h^{-1}$. For these flows, it is crucial to provide information on the genesis of bubble trains and on the bubble behavior in microchannels, according to the flow conditions (flow rates and fluid properties) explored. This section presents the results of investigations of biphasic flow in microchannels using a high speed camera. The frequency used is a compromise that allows distinguishing bubbles having a size larger than a few pixels (i.e. of the order of 50 µm, knowing that the pixel size is 16.4 µm) while ensuring that the exposure time (1 µs) does not bias the observation of their morphology. During the time exposure of 1 µs, a particle can make a maximal displacement of 27 µm, taking into account for the average velocity in the outlet microchannel corresponding to the highest investigated flowrate, i.e. 24 L h^{-1}. At this flowrate, some images may seem to be slightly out of focus; this is due to the fact that the image frequency is no more perfectly fitted to the speed of the fluids. Choosing a higher image frequency would imply having a smaller image resolution. Using the visualizations conducted, the gas/liquid flow pattern are determined as a function of the fluids flow rates and liquid viscosity. Then, the effects of fluid flow rates on the size and morphology of the bubble, the eventual effect of the viscosity of the liquid and also of the presence or absence of protein on the flow within microchannels are investigated.

Table 2 : Ranges of operating conditions in the microchannels and characteristic flow numbers, calculated in the outlet microchannel, for a WPI3X035 liquid base and nitrogen, 20 °C.

Fluid	Parameters	Cross 500	Cross 600
	$\mathbf{D_H}$ (m)	5×10^{-4}	6×10^{-4}
Liquid	$\mathbf{Q_L}$ ($L.h^{-1}$)	4.2– 24	
	Liquid pressure at feeding pump P_l (10^5 Pa)	4-13	
	$\mathbf{U_{S,L}}$($m.s^{-1}$)	4.7 – 26.7	3.2 – 18.5
	$\mathbf{t_{residence,L}}$ (ms)	4.2 – 0.75	6.1 – 1.1

	$\dot{\gamma}$ **(10^5 s^{-1})**	1.1 -4.3	0.62 - 2.5
	Re_L (-)	119 – 690	101 – 575
	Ca_L (-)	0.105 – 0.61	0.077 – 0.42
	We_L (-)	255 – 8.4×10^3	147 – 4.8×10^3
	Bo_L (-)	5.8×10^{-2}	8.3×10^{-2}
Gas	**Q_G** ($g.h^{-1}$)	5 – 80	
	Gas inlet pressure P_G (10^5 Pa)	1 – 10	
	Q_G ($L.h^{-1}$) at P_G	4 – 67	
	$U_{S,G}$ ($m.s^{-1}$) at P_G	4.6 – 74	3.2 – 51
	$t_{residence,G}$ (ms) at P_G	4.3 – 0.27	6.3 – 0.39
	Re_G (-) at P_G	160 – 2540	130 – 2120
	Ca_G (-) at P_G	1.8×10^{-3} – 6.3×10^{-2}	7.1×10^{-3} – 5.3×10^{-2}
	We_G (-) at P_G	0.61 – 97	0.35 – 56
	Bo_G (-) at P_G	7.1×10^{-3} – 7.1×10^{-2}	9.6×10^{-5} – 9.6×10^{-4}

3.1. Flow patterns

When the gas and liquid are injected simultaneously into a pipe, the structure of the mixture depends on their properties and also on the geometry of the pipe (inclination, diameter, roughness) (Kleinstreuer, 2003). In the tested microsystems (cross 600 and cross 500), flow patterns are identified by using two kinds of observations: respectively the aspect of foams produced at the outlet of the process, and the visualizations in the cross slot microsystem using the high speed camera. It should be recalled that two pipes of respectively 1.6 mm and 10 mm in diameter and approximately 4 m long each are arranged at the output of the cross for a gradual release of pressure. If the expansion is too quick, the pressure balance in the cross is different and the flow transitions are skewed.

As explained above, the regime transitions are visually determined at the outlet of the process. The same experimental procedure was applied in the two micromixers. For a given value of the liquid flow-rate, the gas flow-rate is decreased monotonically starting from the maximum value, where the slug flow is observed. Once

the gas plugs disappear, the corresponding gas flow-rate is recorded as well as pressure drop and gas injection pressure. Known volumes of produced foams are weighed to determine the experimental void fraction (see eq. 5). The observed biphasic flow patterns are plotted on a classical coordinate flow map ($U_{S,G}$, $U_{S,L}$). In this study, the limits correspond to the transition between the flow patterns observed in the experimental field; they are determined using six pairs of flow rates (Q_G, Q_L).

It may be noted that at low gas flow, the gas pressure is too low for the two fluids to come into contact. Therefore, the liquid flows through the other three channels, preventing the gas from entering the cell. This is a technological limit due to the system geometry and pressure unbalance.

Two flow structures are visually observed according to the aspect of the foam at the outlet of the process:

- *Dispersed flow* is identified at intermediate gas flow, where the two fluids mix perfectly. All the gas introduced is incorporated in the foam. The void fraction of the resulting foam can directly be determined from the fluids flow rates.
- *Pulsed flow is* characterized with gas slugs that appear when the gas flow is too high. The void fraction of the foam is no longer directly controlled by fluid flows. Pulses of foam with pockets of gas are observed. For the same liquid flow rate, the pulsation is enhanced when the gas flow rate is high.

Visualizations within the outlet microchannel using the high speed camera confirm these different flow transitions. It was formerly verified with the tested solutions that no hysteresis effect occurs if the flow rates are studied in a random way (thanks to the non-thixotropic behavior of the solutions). **Fig. 4** shows examples of the behavior of the fluids in the mixing zone respectively with dispersed flow pattern and slug flow pattern, with increasing gas flow intensity. Liquid phase appears transparent in the image capture while the interfaces with bubbles are dark; thus a good contrast is obtained. According to the flow visualization at the dispersed flow (**Fig. 4-a**), bubbles formed at the cross junction do not merge during their travel in the outlet channel. In contrast, when slug flow appears the bubbles quickly come together after their formation and progressively merge to form a continuous flow of gas at the end of the microchannel. It may be noticed that, despite the poor quality of photos presented in **Fig4-c** and **Fig 4-d**, the biphasic flow observed at the end part of the microchannel is rather closed to churn flow than to annular slug flow, as it is more chaotic and distorted than annular slug flow. Brauner and Barnea (1986) have formerly studied the slug/churn transition in upward gas/liquid flow in columns with internal

diameters at the centimeter scale; they mentioned that churn flow is sometimes referred as to pulsating annular flow or annular and slug pattern and that it is difficult, at high liquid velocities, to discriminate visually between churn and slug flow.

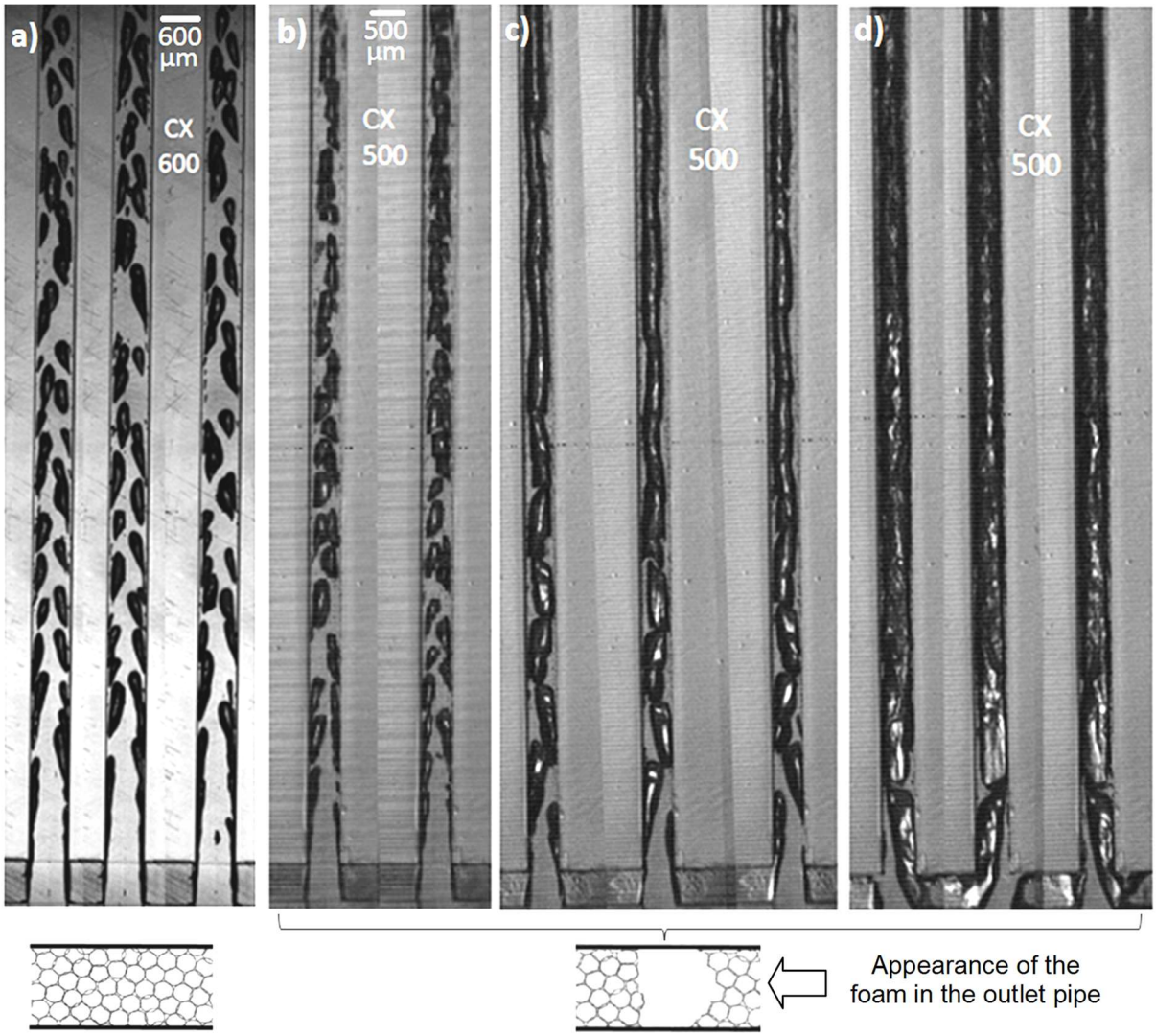

Fig.4 : Example of visualization of flow regimes in microchannels (Frequency 5kHz, 1µs exposure time, 1 pixel = 17 µm, 0.2ms between each successive image) for WPI3X02 liquid solution with Q_L = 6 $L.h^{-1}$: a) dispersed flow pattern; Q_G = 15 $L.h^{-1}$ and α=0,71 - b) slug flow pattern with low pulsations; Q_G = 25 $L.h^{-1}$ and $\alpha_{theoretical}$ =0,81 - c) slug flow pattern with moderate pulsations at the end of the process; Q_G = 35 $L.h^{-1}$ and $\alpha_{theoretical}$ =0,85 - d) slug flow pattern with significant pulsations at the end of the process ; Q_G = 50 $L.h^{-1}$ and $\alpha_{theoretical}$ =0,89.

The transitions between the two observed flow patterns are recapped and represented in a flow chart for the cross 600 (**Fig. 5**) and cross 500 (**Fig. 6**) with only two solutions of different viscosities, for clarity. Their determination is relatively easy and reproducible, with about 8% uncertainty only in the gas flow rate. **Fig.5** and

Fig.6 presents these transitions using superficial velocity of phases; superficial velocity of gas being calculated at atmospheric pressure.

The lower limit of the dispersed flow is represented by a dotted line while the solid line corresponds to the upper limit. The dispersed regime is observed in a relatively narrow zone characterized by a range of the void fraction α ~ [0.35 to 0.51] with WPI3X05 and α ~ [0.5 to 0.7] with WPI3X02 in the cross 600 (**Fig. 5**). In the present case, both limits shift to lower fluid velocities when the viscosity of the liquid phase increases. The same trend was formerly observed using SMX (SULZER^{TM}, Switzerland) (Laporte et al. 2014): a reduction of the maximum void fraction occurs with an increase in viscosity of the liquid phase.

The upper limit of the liquid flow rates differs between the two crosses: for Q_L > 24 L.h^{-1} in the cross 600, the flow become unstable and the liquid flowrate cannot be kept constant, analogously for Q_L > 18 L.h^{-1} in the cross 500. This problem is also encountered with more viscous solutions with different limits according to the cross section: for the cross 500 the flow is totally unstable, even at low flow rates for solutions with 0.5 wt% xanthan or more, while for the cross 600, a stable flow is established with 0.5% xanthan. But for higher concentrations, the flow is unstable in any flow condition. As regards the less viscous solution, containing 0.2% of xanthan, the obtained foams are not stable enough and the liquid drains too quickly. A flow rate limitation is also encountered when the gas pressure reaches 10 bar. Thus, there are physical limitations with respect to the characteristics of the liquid (flow rate and viscosity) due to the micromixer configuration.

As mentioned by Zhao and Middlelberg (2011) in their review, Zhang and Wang (2009) previously investigated the transition between flow patterns in confined microfluidic glass T-junction channels pointing out that they depend on both gas and liquid flow rates. Zhang and Wang (2009) noticed that only a given range of gas inlet pressure allows forming regular bubbles. Under a minimum pressure, no bubble can be generated. On the other hand, if a too high gas pressure is applied, these authors indicate that “layered laminar flow of gas and liquid phases would be triggered”.

Concerning the positions of the limit dispersed flow/slug flow observed in our work, it is difficult to compare them to other studies concerning biphasic flow in microchannels, as the range of gas and liquid velocities investigated are rather high. Triplett et al. (1999) proposed a flow chart for a biphasic air/water system in a circular pipe with 1 mm in diameter. The range of velocities studied is large enough to make a comparison. The position of the limits of the dispersed flow, or so-called bubbly flow, in their work is rather in accordance with our results. But Triplett et al (2014) describes another limit, for larger gas velocities, which concerns slug and churn flow regimes. This limit is not observed in our work. It may be emphasized that the flow typology

shows a transition along the microchannel itself for flow conditions corresponding to the limit of dispersed flow (see **Fig. 4 b**). Brauner and Barnea (1986) discussed on churn/slug transition. Despite the fact that their work is based on columns with internal diameter of the order of one to several centimeters, the presented flow charts encounter several decades of velocities (about 0,001-10 m/s for the liquid and 0.01-100 m/s for the gas) which may be of interest for a comparison. The authors propose a predictive model for the churn/slug transition which is in particular based on a simple criterion. In the case of vertical pipes, "the transition to churn flow is postulated to occur when the void fraction within the liquid slug reaches the maximum volumetric bubble packing, i.e. 0.52". The authors also studied and discussed about the effect of inclination of the tube; they concluded on the absence of the churn pattern at relatively low liquid flow rates in shallow inclinations (including horizontal position). However, this conclusion does not seem to be so evident due to the difficulty of characterizing flow patterns at high fluids velocities. In our case, the upper limits for dispersed flow are observed with void fraction superior or equal to 0.52. The most interesting is that the location of these limits are in the same area and have a similar shape than those presented in the flow charts of Brauner and Barnea (1986) for vertical tube. Moreover, as said, the flow visualization in the microchannel is in favor of a transition of dispersed flow/churn flow rather than dispersed flow/slug flow after these limits. The locations of the limits and the visualized flow pattern indicate that the flow charts presented in **Fig. 5** and **6** are closer to flow charts obtained with vertical flows in pipes than with horizontal ones. This discussion would need to be confirmed, with flow visualization at higher frequency of image acquisition, if possible, and/or with a better resolution of images.

Fig. 7 allows comparing the limit between dispersed flow regime and churn or plug flow regime observed in the cross 500 and in the cross 600 using a dimensionless number for each phase; Reynolds number is calculated in the conditions of flow at the entrance of the mixing microchannel. As can be observed, using a smaller microchannel hydraulic diameter allows shifting the flow regime transition to upper gas Reynolds number. This is due to a higher needed pressure of gas injection.

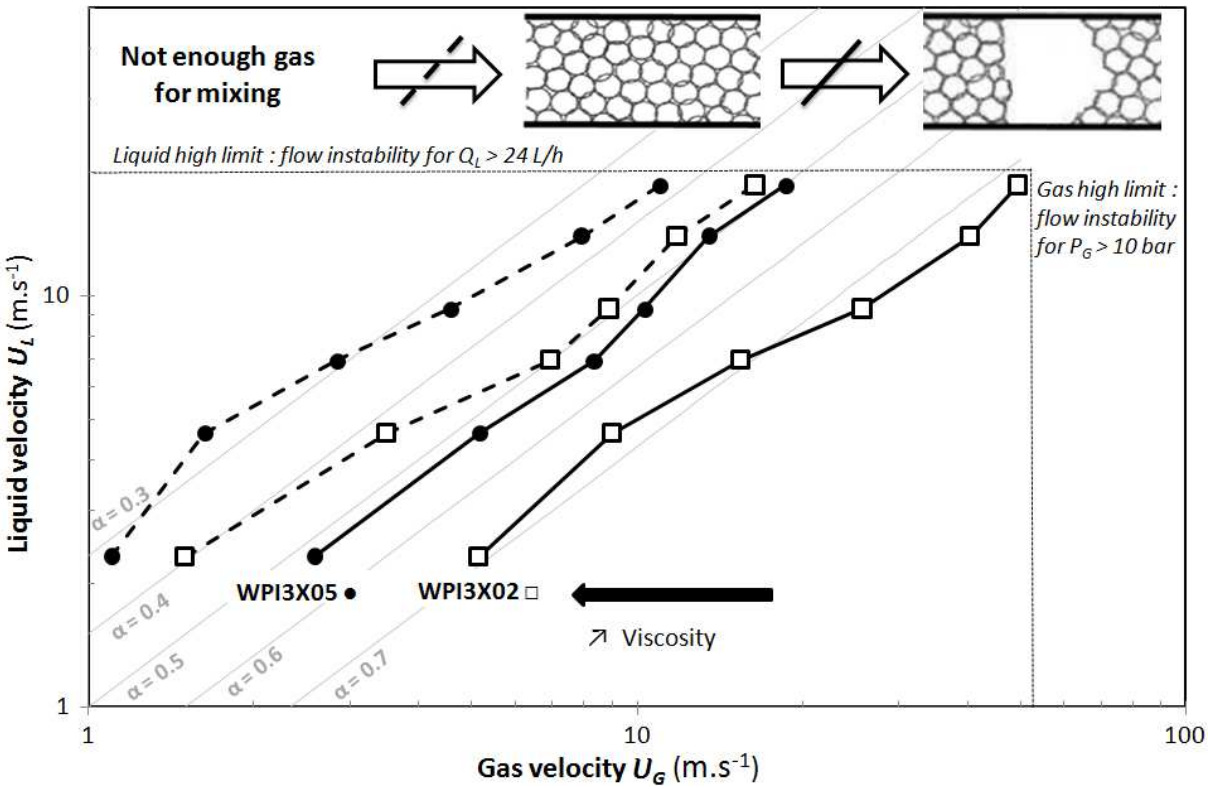

Fig.5: Flow regimes transition in the cross 600 for two liquid solutions: WPI3X05 and WPI3X02. The velocity of gas is given at atmospheric pressure.

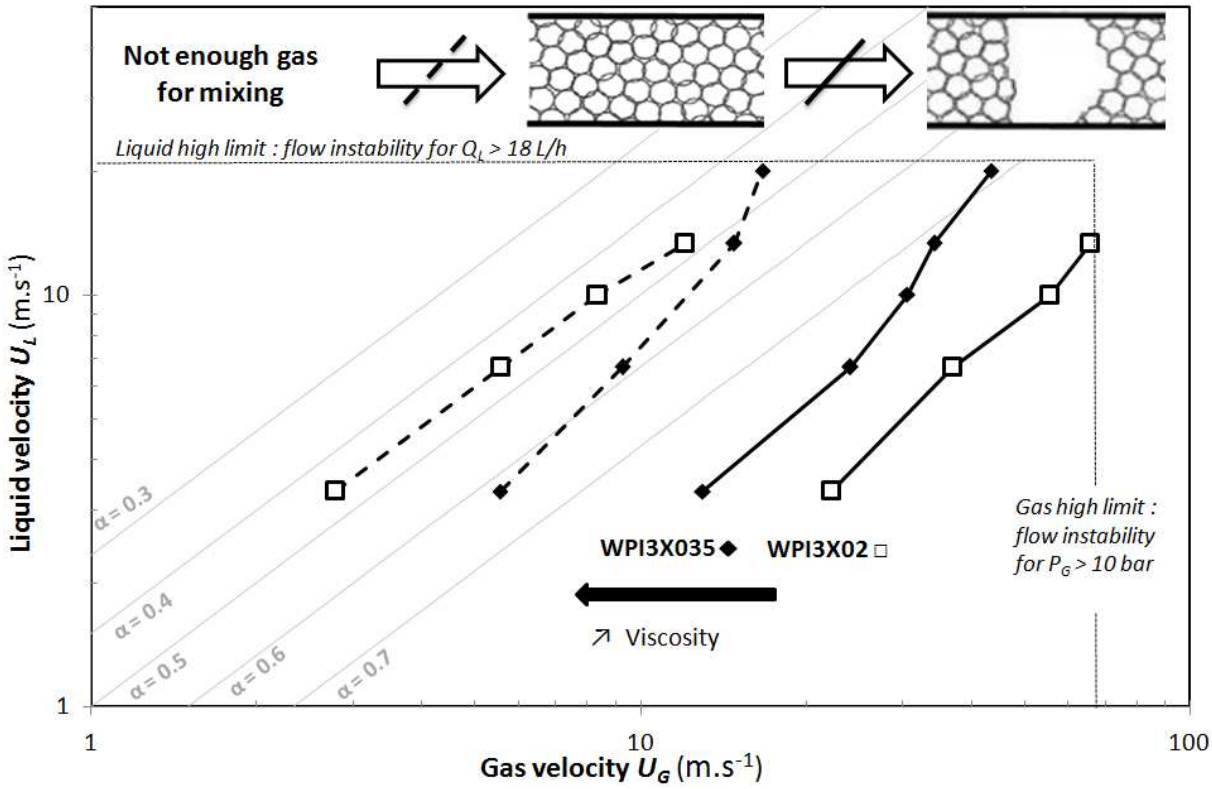

Fig. 6: Flow regimes transition in the cross 500 for two liquid solutions (WPI3X035 and WPI3X02). The velocity of gas is given at atmospheric pressure.

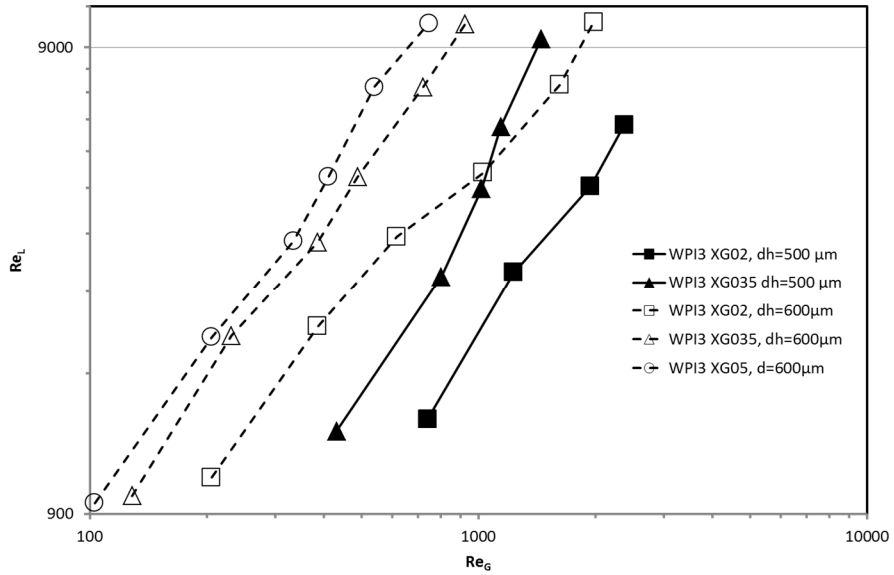

Fig. 7: Comparison of the limit between dispersed flow regime and churn or plug flow regime observed in the cross 500 and in the cross 600. Reynolds number is calculated in the conditions of flow for each phase at the entrance of the mixing microchannel.

Using these flow charts, it is possible to determine the operating conditions providing a total control of the amount of gas incorporated into the foam. **Fig. 8** shows theoretical (Eq.3) and experimental (Eq.5) values of void fractions corresponding to the flow boundary between slug and dispersed flow patterns (straight black lines on **Fig.5** and **Fig. 6**). This shows the accuracy of the control of the fraction of gas incorporated into the foam, and this for a rather wide range [0.5 to 0.87] considering the complementarity of the two microsystems tested.

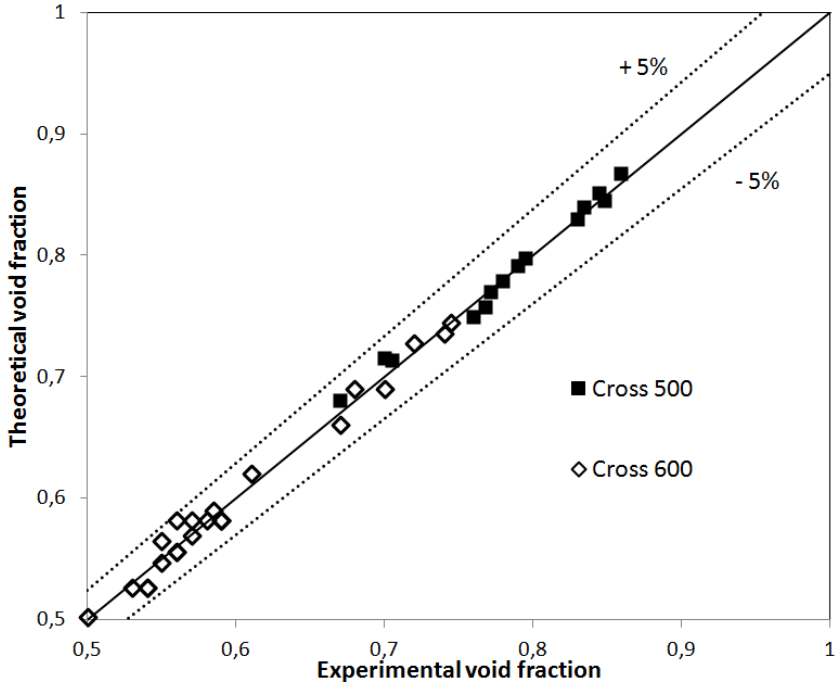

Fig.8: Control of the void fraction in the microchannels.

3.2. Visualizations of the flow in the outlet microchannel

The tested configuration which consists in using one inlet channel for the liquid and the two perpendicular channels for the inlet of the gas enhances a kind of flow focusing at the crossing region. But usually, flow focusing is related to a configuration where the phase to be dispersed is feed in the inlet channel which is in alignment with the outlet channel. As can be observed in the photos presented in this contribution (see **Fig. 4** and **Fig.9**), the liquid acts as a plug which laminates the gas. Bubbles are alternatively formed on each gas inlet. As can be observed in **Fig.4**, the regime of bubble formation in the dispersed flow regime is the jetting one. According to Anna (2016), over a Ca_L value of 0.1, the jetting regime governs the formation of bubbles. As can be seen in **Table 2**, in this study most of the value of Ca_L are larger than 0.1.

453

454 *3.2.1. Surfactant effect of proteins*

455 In order to observe the effect of the proteins on the shape of bubbles, solutions at 0.5 wt % of xanthan
456 respectively with and without WPI were used. The operating conditions ensure a non-pulsed regime in both
457 cases and examples of resulting images are aggregated in **Fig. 9**.

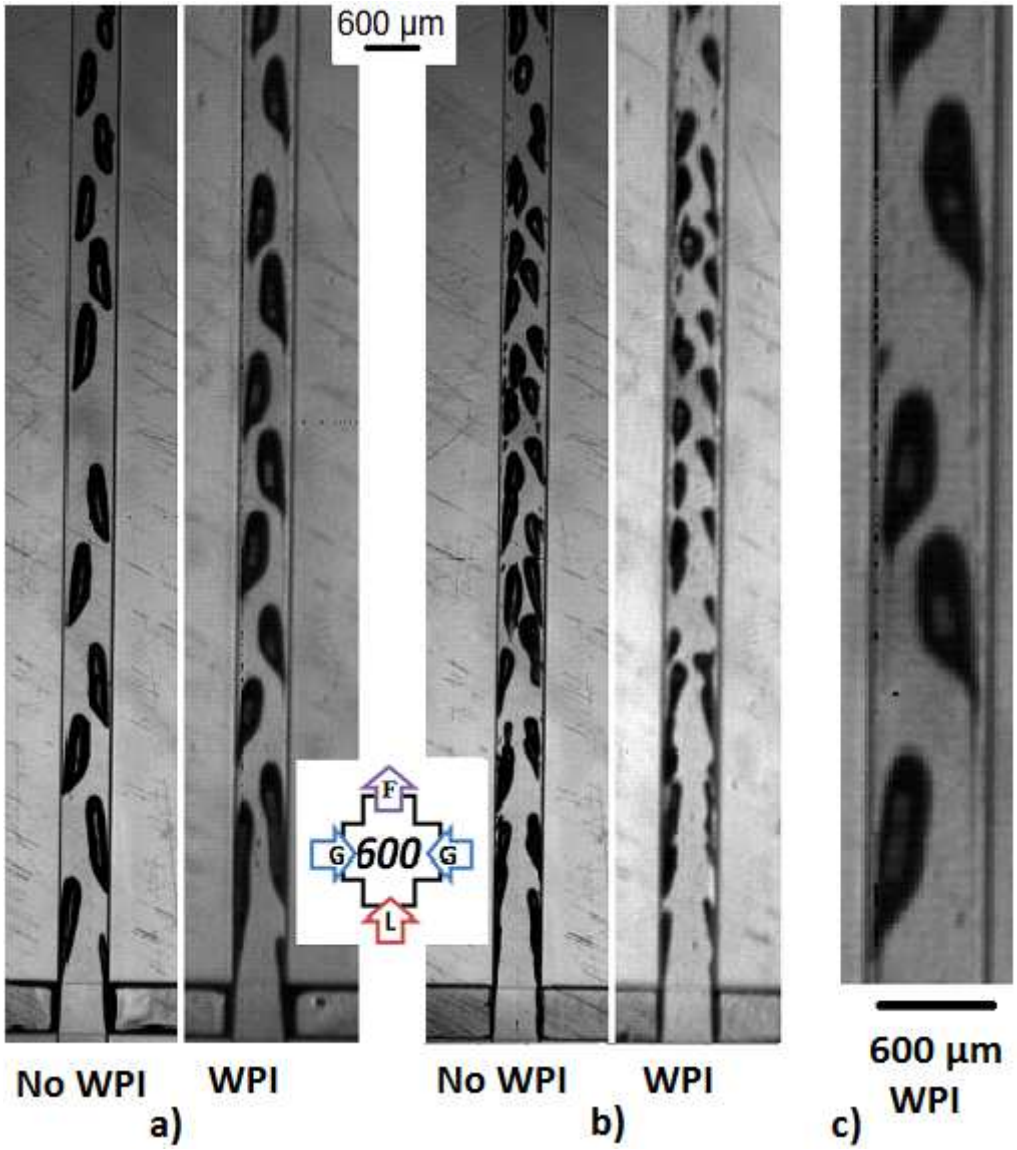

458

459 **Fig.9:** Mixing in the cross 600 cell with or without WPI (XG = 0.5 wt%), in dispersed regime, for
460 different liquid flow rates, (1 kHz, acquisition time 1µs, 1 pixel = 16.4 µm). a) Q_L = 6 L.h^{-1}, Q_G = 7 L.h^{-1}; b)
461 Q_L = 24 L.h^{-1}, Q_G = 25 L.h^{-1}; c) zoom in the channel where tip streaming is observed (flow conditions
462 corresponding to the second photo from the left).

463

464 The bubbles appear to have a substantially similar size with or without protein, but their shapes present some
465 differences (**Fig.9.a and Fig.9.c**). In the presence of protein, the bubbles are slightly more rounded at the
466 upstream side. On their downstream side, they develop a "tail" which could be attributed to the surfactant
467 character of proteins. It can be assumed that proteins are concentrated at the back of the bubble, probably under
468 the pressure differential prevailing effect between the front and rear of the bubble, where they promote, by
469 lowering the surface tension, stretching and fragmentation of the bubbles. This phenomenon is known as "tip
470 streaming" and has been observed with emulsions (Leonhard 1966; Taylor 1934). For Leonhard's unpublished
471 work, refer to Drenckhan and Saint-Jalmes (2015). Also, de Bruijn (1993) proved that this drag is indeed caused
472 by surface tension gradients, the droplets being saturated with surfactants. Fluids without surfactants present no
473 tip streaming, as observed in our trials. As can be observed (**Fig.9.a**), the bubbles progressively reach the center
474 part of the channel but they mainly pass through the channel close to the wall, where a high velocity gradient
475 promotes elongation of the tails of bubbles.
476 At higher speed (**Fig.9.b**), it is more difficult to quantify precisely the difference between the bubbles obtained
477 with or without WPI. Despite the relative similarity of the fluid distribution in the outlet microchannel in these
478 trials, i.e., with or without protein, it should be noted that no stable foam is produced at the outlet of the process
479 if no protein is added to the solution. In the presence of protein, the device is able to produce foams whose
480 characteristics are described in a former paper (Laporte et al., 2016). In this work, it has be shown, even with
481 void fractions below the maximum packing (i.e. till 0.55), that the foam is exploitable from a rheological point of
482 view, while remaining stable for several hours at least.
483
484 *3.2.2. Effect of flow rates*
485 **Fig. 10** compares the flow at different flow rates of the same liquid phase and at constant gas fraction.
486 In these trials a salted solution is used. Previous experiments (Laporte et al., 2016) have highlighted the positive
487 impact of NaCl addition (0.2M) on the stability of foams at short and large times. This could be related to the
488 denser and more compact interfacial protein film formed, due to the reduced electrostatic repulsion between
489 proteins. As can be qualitatively observed on the photos (**Fig. 10**), the gas bubbles formed in the microsystem
490 decrease significantly in size with increasing fluid flow rates. No systematic quantification of the size of the
491 bubbles in the microchannel is proposed here as it would not be accurate, due to the low resolution of the
492 pictures. At higher flow rates, it is more difficult to observe and describe what is actually happening in the
493 microchannel: the size and shape of bubbles are more heterogeneous; clusters of bubbles appear along the outlet

channel and organization of bubbles gets more spread in the channel section which seems to indicate a better micromixing. Using this type of flow for bubbles production at this scale of systems is rather unusual, as in the published works, the bubbles are usually generated individually at a lower flow rate, each bubble size being generally close to that of the channel width.

For information, it may be noted that the apparent average size of bubbles observed from the high speed imaging in the microchannel appears to be much higher than that of the bubbles in the foam obtained at the outlet of the process, especially when taking into account the pressure expansion along the process (see **Fig 2**, the outlet of the process is located after the visualization cell). As an example, in **Fig. 10** at Q_L=12 L h^{-1} the apparent 2-D size of the bubbles in the outlet microchannel is about 300 µm in width x 600 µm in length whereas the modal bubble size of the foam determined at the outlet of the process, D_m, is 118 µm; moreover, it may be emphasized that the visualization system located at the outlet of the process does not allow to encounter for bubbles smaller than 20 µm. For liquid flow rates above 12 L.h^{-1}, the bubbles are pressed to the wall and break away in a more disordered way in the second half of the channel length. For the higher liquid flow investigated (24 L.h^{-1}), the bubble size distribution observed in the channel becomes wider (**Fig. 10,** third picture from the left). However, at the outlet of the process, the foam presents a narrow diameter distribution. This also suggests that breakup process continues beyond the microchannel itself. Although at this stage no visualization is possible to assess this hypothesis.

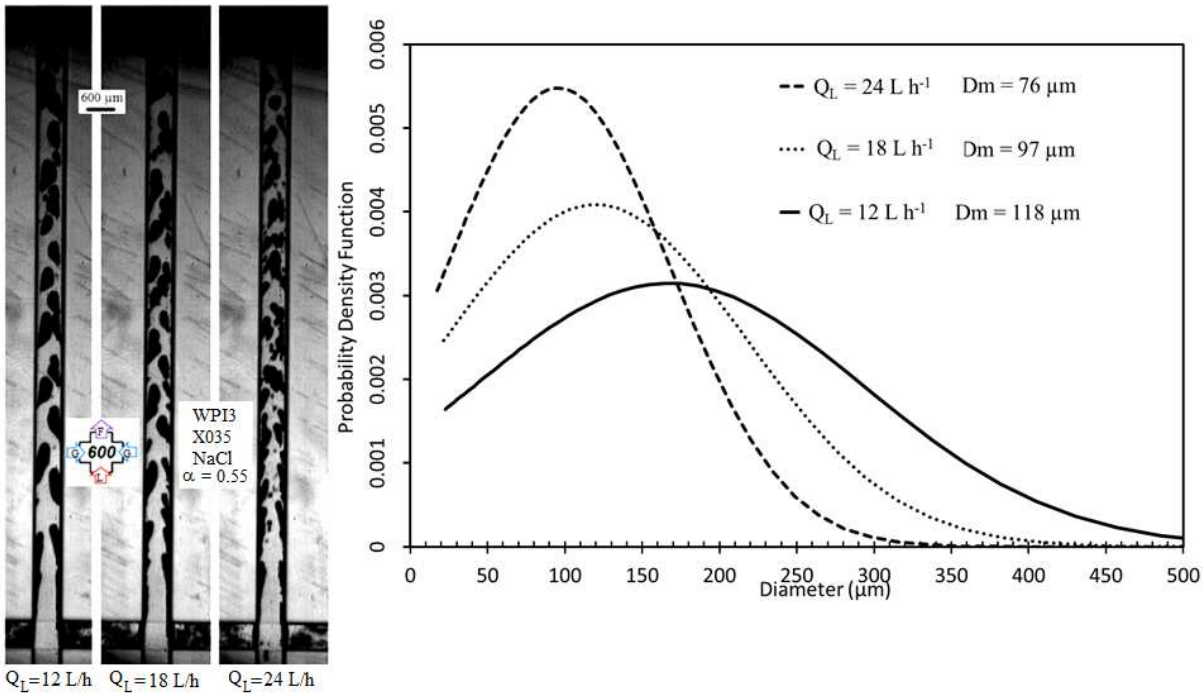

513 **Fig.10:** On the left: images of the flow, for WPI3X035NaCl, α = 0.55, cross 600 at different flow rates (5
514 kHz, acquisition time 1µs, 1 pixel = 16.4 µm). On the right: corresponding lognormal law bubble size
515 distributions observed in the foam at the outlet of the process (The mean square deviation diminishes from
516 85 % to 70% with increasing the flowrate).
517
518 Regarding a description of the flow occurring in this configuration in terms of time evolution, the
519 observation of sequences of images indicate that the bubbles arise alternately and with a remarkable regularity
520 from each gas inlet, in an area where the fluids undergo a high gradient velocity as well as a high pressure
521 gradient. Due to the flow configuration of gas and liquid at the inlet of the microsystems, bubbles are created at
522 the vicinity of the walls. As said, bubbles then circulate close to the wall and progressively migrate in the center
523 of the microchannel. For a given liquid solution, the shape of the bubble is dependent on the flow rate. At low
524 rate of the liquid phase (3 to 6 L/h), bubbles detach from the wall quite quickly and their deformation is similar
525 to that of bubbles observed in previous works in laminar flow regime: they take the appearance of an ogive.
526 However, the observed bubbles are asymmetrical; they have a longer size at the channel side where they are
527 created. In **Fig. 11**, successive photos of the flow captured at 5000 Hz in the cross 500 microsystem operated
528 with the smallest investigated flow rate of liquid allow to distinguish the genesis of the bubbles. In order to
529 follow more easily the bubbles, an artefact (probably an air bubble initially present in the aqueous solution) is
530 marked with an arrow. In these conditions, about 13,300 bubbles appear per second. The kinetic energy of the
531 liquid is about 100 times larger than that of the gas in the two inputs. It allows the liquid to act as a piston on the
532 gas. For a liquid flow rate of 12 $L.h^{-1}$, the size of the bubbles formed is homogeneous and their occurrence
533 frequency is perfectly stable over time as seen in **Fig. 12**. This figure gathers four successive images of the flow
534 captured at 0.2 ms intervals for three flow rates, so that it is possible to follow the bubbles in the channel. As an
535 example, a same cluster of bubbles is circled in successive images in **Fig. 12**. A set of bubbles is chosen as a
536 marker. The path and time interval between successive images allows estimating its velocity. This shows that the
537 velocity increases as the bubble moves ahead in the channel. This may be explained by a progressive expansion
538 of the bubbles along the channel as the pressure diminishes (see for example the picture obtained for Q_L= 12 L/h
539 in **Fig. 12**). This implies that the velocity of the liquid is increasing along the channel, as the void fraction is
540 getting higher, thus bubbles are also conveyed at a larger speed. For higher flow rates, like those presented in **Fig**
541 **4-b to 4-d**, this phenomenon favors the bubbles merging which leads to the formation of slugs and to the
542 transition to a slug flow pattern.

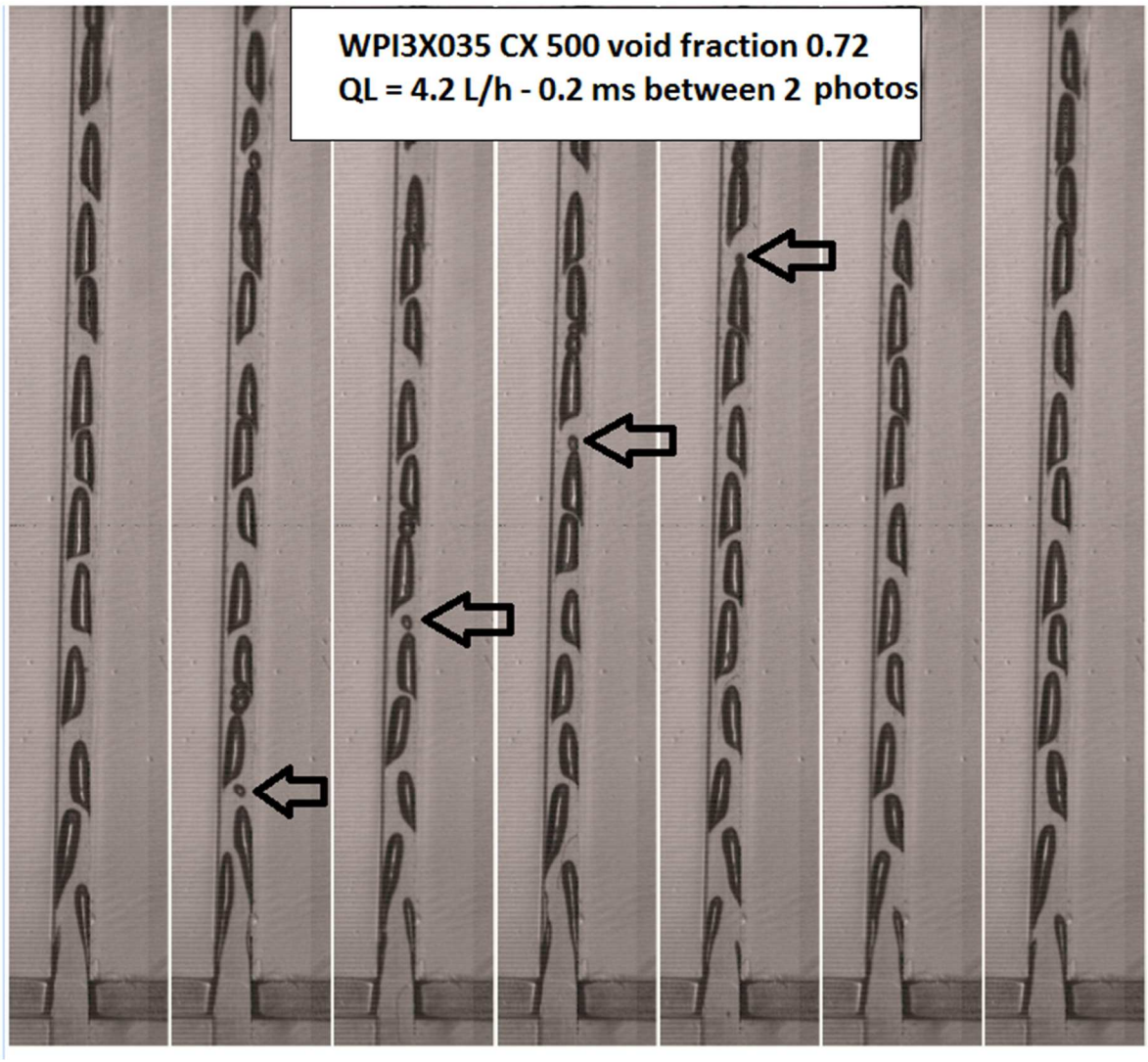

Fig.11: Successive images of the flow in the cross 500, for WPI3X035NaCl, α = 0.72, at Q_L= 4.2 L h^{-1} (5 kHz, acquisition time 1µs, 1 pixel = 16.4 µm, width of the channel = 500 µm).

Fig. 12 also allows us to estimate a bubble apparition frequency. Thus, for a liquid flow rate Q_L = 12 L.h^{-1}, between two images (i.e. 0.2 ms), 7 bubbles are formed which means that about 35,000 bubbles are generated per second. By doubling the fluid flow rates, this number also increases with a factor 2: for Q_L = 24 L.h^{-1} about 70,000 bubbles appear in a second. As can be seen in **Fig. 13**, the bubble frequency varies linearly with the flowrate of the liquid phase as well as with the bubble velocity in the investigated range of liquid flow rates [4.2-24 L/h]. A raw estimation of the mean size of the bubbles can be made. Thus, for Q_L = 12 L.h^{-1}, the bubbles size is about the channel size, i.e. the 2-D section is 600 microns long to ~ 400 µm wide. For Q_L = 24 L.h^{-1}, the length varies a little, ~ 500 µm but the bubbles are more slim, ~ 200 µm wide. At this flow rate, as already mentioned a

large number of bubbles appear stretched and the size dispersion in the channel is more important. It is difficult to get an accurate characterization of the bubbles size along their travel in the channel as their shape is changing significantly.

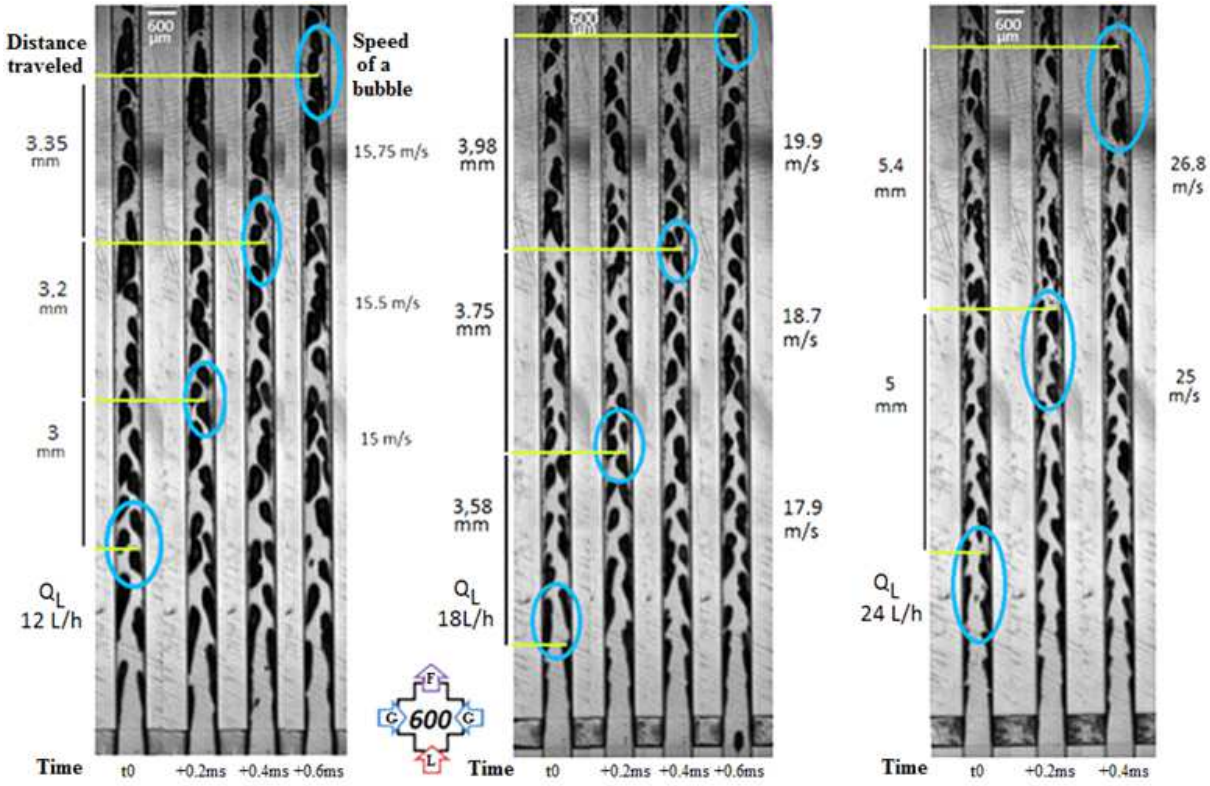

Fig.12: Successive images of the flow, for WPI3X035NaCl, α = 0.55, CX600, at different flow rates (5 kHz, acquisition time 1µs, 1 pixel = 16.4 µm, width of the channel = 600 µm).

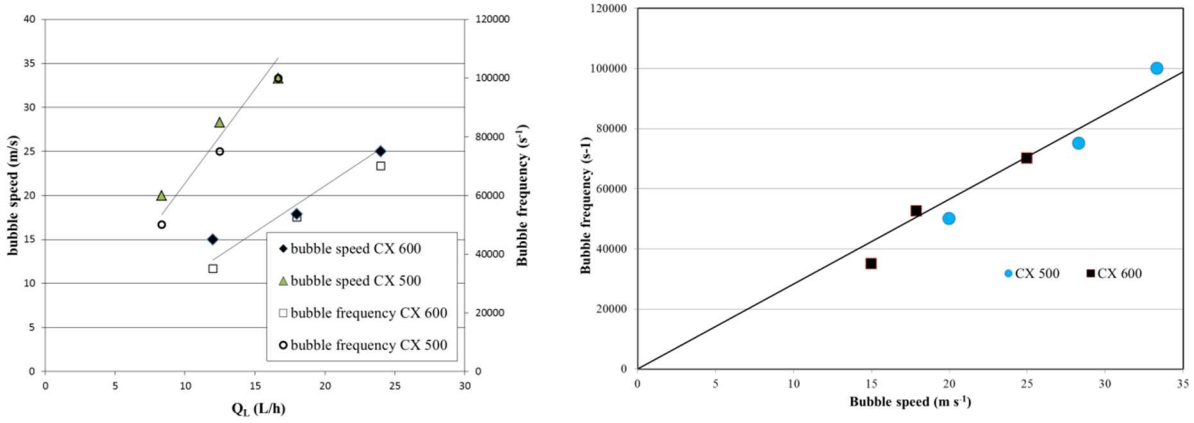

Fig.13: Bubble speed at the entrance of the outlet channel and bubble frequency measured as a function of the flowrate of liquid phase, Q_L (at the left). Bubble frequency is also presented as a function of the velocity of the bubbles in the entrance of the outlet channel (at the right). Data are obtained at a given void fraction ($\alpha = 0.55$) with different flow rates of respectively WPI3X035NaCl (CX 600) and WPI3X035 (CX 500). Images are obtained at 5 kHz and the acquisition time is 1µs.

3.2.3. Effect of xanthan content

To analyze the eventual effect of the xanthan content on the flow topology, two liquid solutions containing respectively 0.5 and 0.2 wt % of xanthan gum, protein-free, were used. The operating conditions ensure to develop dispersed flow with these two solutions. At a given flow rate and depending on the xanthan content, the shape of the bubbles is significantly different (**Fig. 14**). With Q_L = 6 L/h and Q_G = 7 L/h, at the middle length of the channel the bubbles appear to be larger and also more flattened at their back with smaller concentration of xanthan (X02) whereas they appear to be slimmer with a higher xanthan content, and thus a slightly more viscous liquid (X05). In the same pictures, it can be observed that, at the end of the channel, the apparent section of each bubble is much smaller when the xanthan content is higher (X05). This result is consistent with the trend previously observed, concerning the effect of viscosity on the bubble diameter obtained in the foam at the outlet of a process based on static mixers SMX (Laporte et al. 2015). In this work, it was shown that increasing the xanthan content slightly favors the bubble break-up, as smaller bubble diameters are observed in the collected foam. With Q_L = 24 L.h^{-1}, Q_G = 25 L.h^{-1} (**Fig. 14**), as formerly mentioned the size distribution of the bubbles is more spread and their dispersion in the channel is more heterogeneous, making a comparison more delicate. However, it may be noticed that the size distribution seems to be less spread with the more viscous liquid phase.

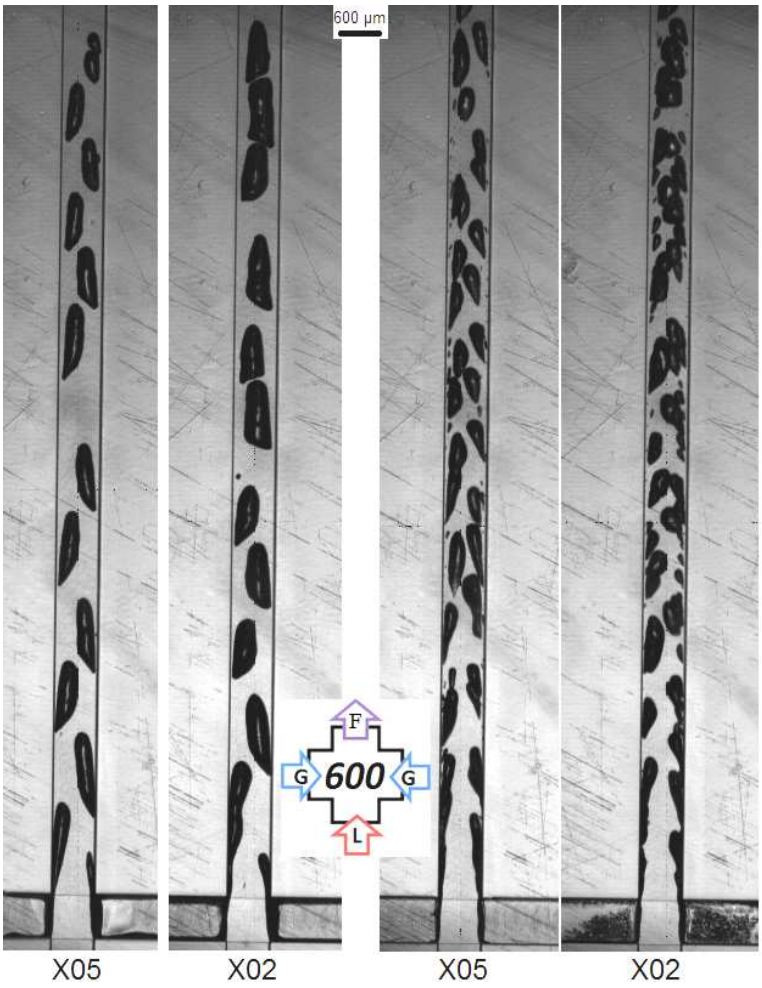

Fig.14 : Mixing in the cross 600 cell for liquid bases with 0.5wt% and 0.2wt% of xanthan (no WPI in these trials), in dispersed regime, for different liquid flow rates (1 kHz, acquisition time 1µs, 1 pixel = 16.4 µm, width of the channel = 600 µm). Two photos in the left: Q_L = 6 L.h^{-1}, Q_G = 7 L.h^{-1}. Two photos in the right: Q_L = 24 L.h^{-1}, Q_G = 25 L.h^{-1}.

4. Conclusion

The gas/liquid mixing at high flow rates, in micro channels is likely to have many interesting perspectives, especially concerning foams formulated for food engineering or cosmetic industry. This exploratory study proposes observations and analysis of an unusual use of microsystems for such a process, as a contribution for a better knowledge and understanding on the genesis of bubbles.

This study has identified two flow patterns in the microchannels, dispersed flow and churn or slug flow; only the first one allowing the total incorporation and controlled gas. The operating limits of these microsystems

606 have been determined. The extent of dispersed flow regime is shown to be dependent on the content of xanthan
607 and thus on the rheological properties of the liquid phase. The section of the microchannels also has an influence
608 on the extent of the dispersed flow regime. Reducing the size of the microchannel provides greater shear rates,
609 but this obviously comes at the expense of a narrower available liquid viscosity range. It was impossible to
610 obtain a stable flow with concentration of xanthan greater than respectively 0.5 wt% in the cross 600 and 0.35%
611 in the cross 500. The limit of fine bubbles formed is thus shown to be dictated by viscosity threshold
612 corresponding to a stable flow.

613 Concerning the effect of the surfactant used, WPI, tip streaming has been observed. The effects of the
614 liquid flow rates on the bubble size and their frequency of appearance in the outlet channel were also studied;
615 this latter was shown to vary linearly with the flow rate of liquid. When increasing the flow rate, a narrower
616 distribution of bubble size was clearly observed in the foam produced at the outlet of the process, whereas the
617 opposite situation was noticed in the outlet microchannel.

618 The microsystems such as these used in this study are an interesting tool for research and development
619 because, due to a residence time of about a millisecond, the system implementation is very fast. A permanent
620 flow at dispersed flow pattern is quickly reached and the fluids volumes required for these tests are small. These
621 systems allow considering promising trials with molecules that are currently prohibitively expensive for
622 industrial use. However, fractioning mechanisms in the whole microsystem and process remain incompletely
623 elucidated. This study has revealed how the bubbles trains were generated in the channels, which is a first step in
624 the knowledge of the foam formation in such continuous processes. It also allowed describing the typology of
625 the flow within the channel for different flow rates and roughly characterized the shape and size of the bubbles.
626 The link between the characteristics of these bubbles trains and foam properties obtained (bubble size
627 distribution at the outlet of the process) is not yet fully established. It implies, in particular, to study the effect of
628 subsequent parts of the process, like outlet tubes in which a progressive pressure relaxation of the foam is
629 obtained. Concerning the microsystem itself, the implantation of the output ports at 90° may have an impact on
630 the elongation and further splitting of the bubbles: this effect has not been highlighted separately and should
631 need additional work. Next work will focus on this effect of the outlet bend, and investigate for scaling laws with
632 the dimensional parameters to help for the exploitation and design improvement of the microchannel systems.
633
634 **Acknowledgments**
635

636 This program has been supported by a research grant of the French government (MENRT) and FEDER funds.
637 The technical support of Oniris-GPA, especially Luc Guihard and Christophe Couëdel, are deeply acknowledged
638 for the perfect implementation of the experimental set-up.
639
640

641

642 **References**

643

644 Ait Mouheb, N., Solliec, C., Montillet, A., Havlica, J., Legentilhomme, P., Comiti, J., Tihon, J (2010) Flow
645 characterization in T-shaped and cross-shaped micromixers. *Microfluidic Nanofluidic Journal,* 10,
646 1185–1197.

647 Anna, S. L. (2016). Droplets and Bubbles in Microfluidic Devices. Annual Review of Fluid Mechanics, 48(1),
648 285–309.

649 Brauner N., and Barnea D., (1986) Slug/churn transition in upward gas-liquid flow. *Chem. Engn Sci*., 4, 159-
650 163.

651 Benichou, A., Aserin, A., Lutz R., Garti N. (2007) Formation and characterization of amphiphilic conjugates of
652 whey protein isolate (WPI)/xanthan to improve surface activity. *Food Hydrocolloids* 21: 379–391.

653 Besagni, G., Brazzale, P., Fiocca, A., Inzoli, F., (2016) Estimation of bubble size distributions and shapes in two-
654 phase bubble column using image analysis and optical probes. Flow Meas. Instrum. 52, 190–207.

655 Chen, C.P., Zhu, Y.G., Leech, P.W., Manasseh, R. (2009) Production of monodispersed micron-sized bubbles at
656 high rates in a microfluidic device. *Applied Physics Letters 95*, 144101.

657 De Bruijn, R.A. (1993) Tip streaming of drops in simple shear flows. *Chemical Engineering Science* 48, 277–
658 284.

659 Dickinson, E. and Walstra, P. (2011) Food Colloids and Polymers: Stability and Mechanical Properties,
660 Woodhead Publishing Limited, p. 225.

661 Drenckhan, W., Saint-Jalmes, A. (2015) The science of foaming. *Advances in Colloid and Interface Science*.

662 Engler, M., Kockmann, N., Kiefer, T., Woias, P. (2004) Numerical and experimental investigations on liquid
663 mixing in static micromixers. *Chemical Engineering Science,* 101: 315–322.

664 Famelart, M.H., Guyomarc'h, F., Morand, M. and Novales, B. (2011) Agrégation protéique et propriétés
665 gélifiantes et moussantes des protéines laitières – quoi de neuf sur le plan des connaissances ? *Innovations*
666 *Agronomiques,* 13, 117-132

667 Galletti, C., Roudgar, M., Brunazzi, E., Mauri, R. (2012) Effect of inlet conditions on the engulfment pattern in a
668 T-shaped micro-mixer. *Chemical Engineering Journal, 185-186*, 300-313.

669 Garstecki, P., Fuerstman, M.J., Stone, H.A., Whitesides, G.M. (2006) Formation of droplets and bubbles in a
670 microfluidic T-junction—scaling and mechanism of break-up. *Lab on a Chip, 6*, 437–446.

671 Guimarães Pelegrine, D., de Moraes Santos Gomes, M. (2008) Whey proteins solubility curves at several
672 temperatures values. *Ciência E Natura, 30*: 17–25.
673 Huchet F., Havlica J., Legentilhomme P., Montillet A., Comiti J., Tihon J. (2008) Multi-scale analysis of
674 hydrodynamics inside a network of crossing minichannels using electrodiffusion method and PIV
675 measurements. *International Journal Heat and Fluid Flow 29*: 1411-1421.
676 Kleinstreuer, C. (2003) Two-Phase Flow: Theory and Applications, first ed. Taylor and Francis, New York.
677 Kockmann, N. (2008) Transport phenomena in micro process engineering. Springer.
678 Kumar, V., Paraschivoiu, M., Nigam, K.D.P. (2011) Single-phase fluid flow and mixing in microchannels.
679 *Chemical Engineering Science, 66* (7), 1329–1373.
680 Laporte, M., Loisel, C., Della Valle, D., Riaublanc, A., Montillet, A. (2014) Flow process conditions to control
681 the void fraction of food foams in static mixers, *Journal Food Engineering*, 128, 119–126.
682 Laporte M., Della Valle D., Loisel C., Marze S., Riaublanc A., Montillet A. (2015) Rheological properties of
683 food foams produced by SMX static mixers. *Food Hydrocolloids, 43*: 51-57.
684 Laporte M., Montillet A, Della Valle D., Loisel C., Riaublanc A. (2016) Characteristics of foams produced with
685 viscous shear thinning fluids using microchannels at high throughput. Journal of Food Engineering,
686 173, 25-33.
687 Lee, B.-B., Chan, E.-N., Ravindra, P. and Ahmad, Khan T. (2012) Surface tension of viscous biopolymer
688 solutions measured using the du Nouy ring method and the drop weight methods, Polym. Bull. 69:471–
689 489.
690 Leonhard, H., (1996). Experiments on tip streaming, not published.
691 Nguyen N.-T. (2011). Micromixers: fundamentals, design, and fabrication. - Norwich: William Andrew, Ed. 2.
692 Park J.I., Nie Z.H., Kumachev A., Kumacheva E. (2010). A microfluidic route to small CO_2 microbubbles with
693 narrow size distribution. *Soft Matter, 6*, 630–634.
694 Poux, M., Cognet, P., Gourdon, C. (2015) Green Process Engineering: From Concepts to Industrial Applications.
695 CRC press.
696 Rio S., Legentilhomme P., Comiti J., Montillet A. (2008) Characterization of oil in wateremulsion inside
697 miniaturized systems. In: CHISA 18th International Congress of Chemical Engineering equipment
698 Design and Automation. Praha, Czech Republic.
699 Soleymani A., Kolehmainen E., Turunen I. (2008) Numerical and experimental investigations of liquid mixing in
700 T-type micromixers. *Chemical Engineering Journal, 135*:219–28.

Srisamran C., Devahastin S. (2006) Numerical simulation of flow and mixing behavior of impinging streams of shear-thinning fluids. *Chemical Engineering Science, 61*: 4884–4892.

Sworn G. (2000) Handbook of hydrocolloids. CRC Press. Boca Raton.

Sworn G. (2011) Xanthan gum – functionality and application. Practical Food Rheology.Wiley-Blackwell.

Taylor, G. I. (1934). The formation of emulsions in definable fields of flow, *Proceedings of the Royal Society A*,146, 501 – 526.

Vigneau E., Loisel C., Devaux M.F., Cantoni P. (2000) Number of particles for the determination of size distribution from microscopic images. *Powder Technology, 107*: 243–250.

Xu J.H., Li S., Chen G.G., & Luo G.S. (2006) Formation of monodisperse microbubbles in a microfluidic device. *AIChE Journal, 52*, 2254–2259.

Zhang, Y.X., and Wang, L.Q. (2009) Experimental investigation of bubble formation in a microfluidic T-shaped junction. *Nanoscale and Microscale Thermophysical Engineering,* 13, 228–242.